Vol. 46 — N° 2 06 22 p. 261 – 276

Secondary Ion Mass Spectrometry Reference Materials for Lithium in Carbonaceous Matrices

Zebadiah **Teichert** (1)*, Maitrayee **Bose** (1), Peter **Williams** (2), Richard L. **Hervig** (1) and Lynda B. **Williams** (1)

(1) School of Earth and Space Exploration, Arizona State University, Tempe, AZ, 85287-1404, USA
(2) School of Molecular Sciences, Arizona State University, Tempe, AZ, 85287-1404, USA
* Corresponding author. e-mail: zteicher@asu.edu

Secondary ion mass spectrometry techniques are used to study trace elements in organic samples where matrix compositions vary spatially. This study was conducted to develop calibrations for lithium content and lithium isotope measurements in kerogen. Known concentrations of Li ions (^{6}Li and ^{7}Li) were implanted into organic polymers, with a range of H/C and O/C ratios similar to kerogen, along with glassy carbon (SPI Glas-22) and silicate glass (NIST SRM 612). Results show that Li content calibration factors (*K) are similar for carbonaceous samples when analysed using a 5 kV secondary ion accelerating voltage. Using a 9 kV secondary ion accelerating voltage, *K** factors are negatively correlated with the sample O content, changing ~ 30% between 0 and 15 oxygen atomic %. Thus, to avoid the matrix effect related to O content, using a 5 kV secondary ion accelerating voltage is best for quantification of Li contents based on $^{7}Li^{+}/^{12}C^{+}$ ratios. Under these analytical conditions, Li ppm (atomic) = (132 ($\pm$ 8) × $^{7}Li^{+}/^{12}C^{+}$) × ^{12}C atom fraction of the sample measured. Lithium isotope ratio measurements of SPI Glas-22 and NIST SRM 612 are within uncertainty; however, the organic polymer samples as a group show a 10‰ higher δ^{7}Li than NIST SRM 612.**

Keywords: SIMS, lithium calibration, matrix effects, organic polymers, Li isotopes.

Received 22 Jun 21 – Accepted 09 Dec 21

Lithium matrix effects, defined as the variable instrumental sensitivity due to differences in matrix chemistry, have been identified in several secondary ion mass spectrometry (SIMS) studies of silicate mineral and glass matrices (e.g., Wilson and Long 1982, Hervig *et al.* 2004, Kasemann *et al.* 2005, Jeffcoate *et al.* 2007, Bell *et al.* 2009); however, no previous SIMS studies have attempted to quantify Li content and Li isotopic ratios in carbonaceous matrices. Lithium derived from organic sources has been largely overlooked in the Li geochemical cycle until recently (Lemarchand *et al.* 2010, Williams *et al.* 2013, 2015). Teichert *et al.* (2020) reported that Li isotopic ratios ($^{7}Li^{+}/^{6}Li^{+}$) in kerogen from coal increased linearly with thermal maturity. That study prompted this research to develop appropriate SIMS reference materials for the determination of Li content in organic matrices and to evaluate potential matrix effects on Li isotope ratio measurements.

Isolating kerogen from mineral matter in coal and other hydrocarbon source rocks using acids alters the Li content and isotopic composition (Williams and Bose 2018). Therefore, we used dynamic SIMS for an *in situ* study of Li in kerogen. SIMS generally requires matrix-matched reference materials for interpreting ion ratios. Consequently, the objective of this study was to quantitatively implant Li into a suite of organic polymers with different C-H-O contents, allowing their use as SIMS reference materials for Li content and Li isotopic composition in organic matrices.

SIMS matrix effects and ion-implant reference materials

In SIMS analyses, secondary ions undergo instrumental mass fractionation (IMF) during sputtering, ionisation and transmission through the instrument (Wilson *et al.* 1989). Sputtering and ionisation are the only sample dependent fractionation processes, and measuring different matrices can result in a deviation of ion yields by more than two orders of magnitude in synthetic materials (Andersen and Hinthorne 1972, Deline *et al.* 1978a, Williams 1979a). While the

doi: 10.1111/ggr.12415
© 2022 The Authors. Geostandards and Geoanalytical Research © 2022 International Association of Geoanalysts

physics of sputtering and ionisation processes has been evaluated (e.g., Williams 1979b), an all-encompassing sputtering/ionisation theory that can correct for matrix effects is unavailable. Therefore, to quantify elemental abundances of materials via SIMS, matrix-matched reference materials are best. Similarly, for isotopic measurement, matrix-matched reference materials should be used to avoid misinterpretation of measured ion ratios (e.g., Isa *et al.* 2017).

Because of the difficulty of preparing homogenous solid-phase samples, the use of quantitative ion implantation into a matrix similar to the unknown was developed as a means of preparing reference materials in the 1970s. Researchers studying solar wind implantation used artificial ion implantation to quantify surface concentrations of solar wind implanted elements in a lunar sample (Zinner and Walker 1975, Zinner *et al.* 1976). Deline *et al.* (1978a) investigated the ion yields of five materials (C, Si, Ge, GaAs, Sn) implanted with B, C, O, F, P, As and Sb. They found the ion yields of a given species changed by up to three orders of magnitude depending on the substrate into which the ions were implanted, demonstrating the need for matrix-matched reference materials for quantification of SIMS measurements. For geological samples, implant reference materials have been used to quantify hydrogen, carbon and oxygen in trapped glass inclusions in volcanic rocks (Hervig *et al.* 2003, Regier *et al.* 2016), hydrogen in terrestrial diamonds (Kaminsky *et al.* 2020), nitrogen in upper mantle minerals (Li *et al.* 2013) and chromium in carbonates (Steele *et al.* 2017). Burnett *et al.* (2015) recently reviewed the key parameters for preparation of implant reference materials and methods for implant calibration of geological samples. They demonstrated how to quantify the trace Li content in melilite samples by implanting the minor isotope ^{6}Li directly into the mineral at a known concentration and then measuring both ^{7}Li and ^{6}Li. The terrestrial abundance ratio of ^{7}Li/^{6}Li then allowed the calculation of the ^{7}Li abundance from the known ^{6}Li implant fluence. Williams *et al.* (1983) first demonstrated this technique by implanting deuterium into hydrogenated amorphous silicon films to determine their H content. Franzreb *et al.* (2004) later demonstrated the use of ^{18}O implants to quantify major levels of oxygen in silicon sputtered by $^{16}O^-$ primary ions while backfilling the analysis chamber with various amounts of O_2.

The creation of an implant reference material is achieved by using an ion implanter to generate a high-energy (10–200 keV) ion beam (beam diameter = 0.3 to 0.6 cm) of an isotope of interest and rastering that beam over the surface of the sample to implant a user-defined and uniform areal density (atoms cm^{-2}) and depth of the implant species. The implant results in an approximately Gaussian, subsurface distribution, which allows it to be clearly distinguished from any intrinsic (uniform) level of the same species. Following ion implantation, the depth profiling capabilities of SIMS instruments allow the shape of the implant profile to be determined. The implant profile, together with a measurement of the analysis crater depth using a profilometer, is used to determine the concentration (atoms cm^{-3}) integrated over the implant depth. This procedure will only work well if the sample being implanted is relatively homogenous. The atomic density of the implanted species can be related to the ion intensity by calculating a content calibration factor (see section *Content calibration data reduction*), which can be used to quantify the mass fractions of elements in an unknown sample.

The use of ion implantation to create an isotopic calibration to detect isotope matrix effects is much less mature. Williams *et al.* (1983) used ion implantation to create an isotopic reference material by implanting a silicon wafer with HD^+ ions to produce identical doses of H and D (^{2}H) to determine the isotope fractionation between H^- and D^- secondary ions. Results showed that the fractionation factor for low energy H^-/D^- secondary ions was 1.32 ± 0.01; for high-energy H^-/D^- and for $^{30}SiH^-/^{30}SiD^-$ the fractionation was much smaller: undetectable for H^-/D^- and 0.95 for SiH^-/SiD^-, both with an uncertainty of 3%. More recently, Burnett *et al.* (2015) separately implanted two isotopes of the same element, ^{25}Mg and ^{26}Mg in order to quantify isotopic compositions.

Matrix effects due to the presence of H and O

Perhaps the most important analytical advancement for the study of biological and other organic materials by SIMS techniques was the development of the NanoSIMS 50L (Cameca-Ametek), which has been used widely in the measurement of biomaterials and other organics (Nuñez *et al.* 2017). The NanoSIMS is particularly suited to the measurement of biological samples at the cellular level due to its small primary beam size (down to ~ 50 nm), its multi-collector detection and chemical imaging capabilities. Despite the growing body of literature containing SIMS data from organic materials, absolute quantification of chemical abundances and the determination of matrix effects related to variable concentrations of H or O in carbonaceous materials remain scarce in comparison with studies of inorganic materials. Researchers studying Archaean and Proterozoic organic matter with a primary focus on identifying bio-signatures using carbon isotopes have led the way in quantifying matrix effects in organic matter. SIMS reference materials of graphite (Mojzsis *et al.* 1996, Farquhar *et al.* 1999), diamond (Kaufman and Xiao 2003) and pyrobitumen (Fletcher *et al.* 2008) have been used in these studies. For

 © 2022 The Authors. Geostandards and Geoanalytical Research © 2022 International Association of Geoanalysts

carbon isotopes, House *et al.* (2000) suspected a matrix effect in an algal coal that showed a 10‰ different $\delta^{13}C$ IMF than graphite compared with bulk measurements. Orphan *et al.* (2001) found more than a +10‰ $\delta^{13}C$ matrix effect between microbial cell biomass and graphite. House *et al.* (2000) reported a < 1‰ variation in $\delta^{13}C$ among kerogen matrices with a range of H/C atomic ratios (0.12 to 0.79) while Sangély *et al.* (2005) detected up to a 5‰ matrix effect associated with a larger H/C range (0.04 and 1.74), with higher H contents resulting in lower $\delta^{13}C$ values.

The presence of H and O in inorganic materials has also been found to cause matrix effects, e.g., Hauri *et al.* (2002, 2006) discovered that as the H_2O content of high-silica glasses increased, the D^-/H^- ion ratio decreased (after correction for absolute D/H content). The same effect was reproduced recently (Befus *et al.* 2020), confirming the non-linear influence of increasing H_2O on the D^-/H^- ion ratio. In another study (Othmane *et al.* 2015), variable H_2O content of turquoise minerals was shown to be partially responsible for a variation of up to 20‰ in δD and 7‰ in $\delta^{65}Cu$. These effects are important because H and O are abundant in most carbonaceous compounds and their contents vary widely. Our goal in this study is to evaluate how the presence of H and O atoms present in organic matrices affect the sputtering and ionisation of Li.

Experimental

Ion implantation

Figure 1 shows a Van Krevelen plot for organic source rock types (Van Krevelen 1950, 1961) indicating the range of H/C and O/C compositions of the organic polymers studied relative to the range of different kerogen types and macerals (Van Krevelen 1950, 1961, Van Krevelen and Schuyer 1957).

A variety of chemically homogenous organic polymers were obtained from industrial suppliers (Table 1) for comparison with a pure glassy carbon (SPI Glas-22) and a silicate glass reference material (NIST SRM 612). The elemental abundances of C and H in the polymers were verified using a Perkin Elmer 2400 Series 2 CHNS/O analyser at the Intertek Group PLC (https://www.intertek.com/). The O content was calculated by difference as it was assumed to be the remaining major element in each polymer apart from araldite, which also has ~ 0.06 $g\,g^{-1}$ Cl (https://www.tedpella.com).

The materials (Table 1) were implanted with Li, (among other elements of interest) by Leonard Kroko Inc. (Tustin, CA; krokoimplants.com) in two separate sessions. The first implant

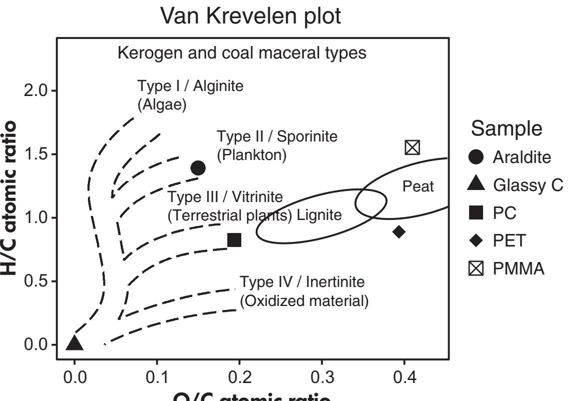

Figure 1. H/C and O/C ratios for polymer and glassy carbon samples used in this study are plotted relative to types of kerogen and kerogen macerals commonly found in coal (Van Krevelen 1950, Van Krevelen and Schuyer 1957). Modified from Van Krevelen (1961) and McCarthy *et al.* (2011).

session was designed to generate reference materials for the determination of the Li content in kerogen (see section *Content calibration*), while the second session was intended to produce Li isotope implant reference materials for kerogen (see *Isotope calibration*, below). Only ^7Li was implanted for the content calibration while both ^7Li and ^6Li isotopes were implanted for Li isotope calibration. Separate samples of the same materials implanted for Li content calibration (Table 1) were implanted for Li isotope calibration, in addition to NIST SRM 612. In both sessions, all materials were implanted simultaneously. Implant fluences can be inaccurate by more than 10% (Heber *et al.* 2014) and, as such, must be absolutely calibrated by implanting a sample that has a known concentration. We used the NIST SRM 612 glass to calibrate the implant fluence of the isotope implant sample batch and used an intercalibration technique (Burnett *et al.* 2015) to determine the fluence of the content calibration implant. The uncertainty in the implantation fluences was within 1.0% of the nominal fluences (i.e., fluences specified to the implanter; see Appendix S1 for details on fluence calibration). The Li concentrations of the un-implanted carbonaceous matrices were near the limits of detection for the SIMS measurement settings described below. A software package for calculating the transport of ions in matter (TRIM; Ziegler *et al.* 2010) was used to determine the implant energy (Table 2) required for the peak concentration at a specified depth.

Each implant species was implanted to generate peak signals near 200 nm depth for polymer samples, such that the entire implant profile could be captured by SIMS depth

© 2022 The Authors. Geostandards and Geoanalytical Research © 2022 International Association of Geoanalysts

profiling. Assuming a Gaussian implant profile, which is reasonable for low energy ion implants (tens of keV; Hofker 1975), the implant fluence can be used to estimate the concentration of the implant species at the peak following Leta and Morrison (1980) as shown in Equation (1):

$$C_p = \frac{0.4\phi}{\Delta R_p} \quad (1)$$

where C_p is the peak concentration of the implant species (atoms cm^{-3}), ø is the fluence of implant species (atoms cm^{-2}) and ΔR_p is the *longitudinal straggle* or standard deviation of the Gaussian implant profile width (cm).

TRIM can be used to calculate the value of ΔR_p, which is the standard deviation of the Gaussian implant profile width, for each material to obtain a desirable implant fluence (± 0.5%) with a known peak concentration. We selected a mass fraction of 1000 μg g^{-1} Li (~ 1.3×10^{20} atoms cm^{-3}) at the implant peak, which corresponds to a fluence of 1.56×10^{15} atoms cm^{-2} in these materials.

The secondary ion yield is affected by sample flatness (Deng and Williams 1989); so, it is essential that the analysed area has a height variation < 1 μm. Thus, prior to implantation, PET, araldite and NIST SRM 612 samples were polished with a final grit size of < 1 μm colloidal silica, while PC, PMMA and glassy carbon samples were delivered with mirror finishes. All samples (cut to 2.54 or 1 cm diameters) were sonified in 1.82% mannitol (a polyhydric alcohol; Tonarini *et al.* 1997) to remove surface adsorbed Li (Williams *et al.* 2012).

Content calibration

The polymer samples (Table 1) along with glassy carbon (SPI Glas-22) were implanted with the major isotope ^{7}Li (92.4%) for Li content calibration. Additional ions were implanted for other investigations (Table 2), but their low abundance is inconsequential to the ^{7}Li sputter yield. SIMS depth profiles were obtained with the Cameca (Ametek) secondary ion mass spectrometer (IMS-6f) using three different analytical setups including different primary ion beams (O_2^- and O^-), impact energies and secondary ion accelerating voltages (Table 3).

The same primary ion accelerating voltage (-12.6 ± 0.01 kV) was used for all analytical setups. To avoid repetition, further discussion will refer to the analytical setup by number (1–3). The change in impact energy and accelerating voltage causes differences in sputter yields and useful secondary ion yields (mass selected ions of a given species detected per atom of that species sputtered; Hervig *et al.* 2006) that are evaluated below (see Appendix S2 for calculations of sputter yield and useful secondary ion yields).

For each analytical setup, a focused primary beam with a diameter of 10–30 μm was rastered across a 125 × 125 μm^2 area using primary ion currents of 30 nA of O_2^- or 60 nA of O^-. A field aperture was used to ensure that only ions coming from a circular area 30 μm in diameter in the middle of the rastered area were counted, eliminating ions from the crater walls. Depth profiling measurements of $^{7}Li^{+}$ and $^{12}C^{+}$ were performed at a mass resolving power (MRP = mass/

Table 2.
Implant session 1

Ion	Fluence (atoms cm^{-2})	Implant energy (keV)
^{7}Li	1.56×10^{15}	17
^{11}B	1.28×10^{15}	40
^{14}N	1.31×10^{15}	52
^{32}S	1.31×10^{15}	110

List of ion implants into araldite, PC, PET, PMMA and glassy carbon (SPI Glas-22) used for this study.
NIST SRM 612 was not included in Session 1.

Table 1.
Implant reference materials H-C-O content and density

Reference material	Chemical formula	H (g g^{-1})	C (g g^{-1})	O (g g^{-1})	Density (g cm^{-3})	Supplier
Araldite 502 epoxy[a]	Proprietary	0.0834	0.714	0.1416	1.1	Luft (1961)
Lexan Polycarbonate (PC)	$(C_{16}H_{14}O_3)_n$	0.0521	0.753	0.1944	1.2	Sabic Innovative Plastics US LLC
Polyethylene terephthalate (PET)	$(C_{10}H_8O_4)_n$	0.0467	0.626	0.3278	1.44	Professional Plastics, Inc.
Polymethyl methacrylate (PMMA)	$(C_5H_8O_2)_n$	0.0776	0.595	0.3249	1.18	SourceOne Displays LLC
SPI-GLASTM 22	NA	< 0.0001	~ 1	< 0.0001	1.5	Structure Probe, Inc.
NIST SRM 612[b]	NA	NA	NA	0.464	2.3	National Institute of Standards and Technology

[a] Araldite contains 0.06 g g^{-1} Cl, in addition to C, H and O.
[b] The reported O content for NIST SRM 612 glass is from Hollocher and Ruiz (1995).

© 2022 The Authors. Geostandards and Geoanalytical Research © 2022 International Association of Geoanalysts

Table 3.
Setup conditions used for depth profiles

Analytical setup	Primary ion	Secondary ion accelerating voltage (kV)	Impact energy per primary atom (kV)
1	O^-	9	21.6
2	O^{2-}	9	10.8
3	O^{2-}	5	8.8

Δmass) of ~ 1000, which is sufficient to resolve $^{11}BH^+$ (~ 12 amu) from interfering with the $^{12}C^+$ peak. Energy filtering (Shimizu 1979) of secondary ions was applied by reducing the sample voltage by 75 V, so that only ions with excess energies of 75 ± 20 eV could be detected, which can reduce molecular interferences. We used energy filtering because it is important for the ion energies detected to be the same for the reference material and unknowns. Energy filtering also reduces the secondary ion signal allowing all ions to be detected using the electron multiplier detector. Sample charging was controlled at each cycle of the analyses using a routine, which scans the sample voltage while monitoring the $^7Li^+$ ion signal and returns the voltage to the value that gives the maximum $^7Li^+$ signal before applying the offset voltage. The efficiency of the electron multiplier detector was maximised for each measurement session using a reference material of known isotopic composition and adjusting the EM gain to get the same ratio (within uncertainty) obtained for each measurement session.

Crater depths were determined by taking the mean of three to four measurements of rastered craters in the *x*, *y* and diagonal directions using a KLA Tencor™ Alpha-Step® 200 stylus profilometer. The crater depth measurements had a $\pm 2s_{\bar{x}}$ precision < 5%.

Content calibration data reduction: The SIMS relative sensitivity factor (Wilson *et al.* 1989) is frequently used for determining the content of elements in matrix-matched materials. However, because the C concentrations in the carbonaceous implant reference materials measured here, and kerogen unknowns vary widely, we define a content calibration factor that takes variations in matrix composition into account.

Dividing the integrated $^7Li^+$ counts in an implant depth profile by the total measurement time spent on $^7Li^+$ (not the total time for the profile) gives a mean count rate for $^7Li^+$ (c/s). Dividing the ^7Li implant dose (^7Li atoms cm^{-2}) by the total crater depth (in cm) gives a mean Li atomic concentration over that profile (^7Li atoms cm^{-3}). A factor that converts count rates to concentration can then be defined as follows:

$$K = (^7\text{Li atoms/cm}^3)/(^7\text{Li}^+ \text{c/s}) \quad (2)$$

This *K* value is specific to the particular matrix and to the analytical conditions used, that is primary ion current, both primary and secondary ion accelerating voltages, primary ion species, mass resolving power and secondary ion energy band pass. To be able to apply a conversion factor to other samples of the same matrix possibly analysed using a different primary ion current value, the $^7Li^+$ count rate in the implant reference material and ^7Li concentration must be normalised to the count rate and concentration for a matrix signal from the target, and ^{12}C was chosen. Because the carbon content varies among different polymers, the ^{12}C concentration must be defined in units of atoms cm^{-3}, which can be calculated as follows:

$$N_C = \left(\frac{(w\, f_m \rho)}{u_m\; NA}\right) \times a_m \quad (3)$$

where N_C is the atom density of the reference isotope (C atoms cm^{-3}), wf_m is the mass fraction of the reference matrix atom in the implant reference material ($g\,g^{-1}$; Table 1), ρ is the material density ($g\,cm^{-3}$; Table 1), u_m is the mean molar mass of reference matrix atom ($g\,mol^{-1}$; 12.011 $g\,mol^{-1}$ for all C), *NA* is Avogadro's number (6.023×10^{23} atoms mol^{-1}) and a_m is the isotopic abundance fraction of reference matrix isotope (0.9893 for ^{12}C).

Using the ^{12}C count rate and concentration, we define a normalised calibration factor *K**:

$$K^* = (\text{atoms cm}^{-3})^* / (\text{c/s})^* \quad (4)$$

where now both the ^7Li concentration and count rate are normalised to the corresponding values for ^{12}C in the implant sample. The ^7Li concentrations in other samples may then be calculated as a fraction of the concentration of ^{12}C by multiplying the $^7Li^+/^{12}C^+$ count rate ratio in the unknown sample by the factor *K**. It is possible that *K** may be affected by some or all of the analytical conditions listed above, as discussed below. Lower *K** values indicate higher sensitivity of the implant ion ($^7Li^+$) relative to the reference ion ($^{12}C^+$).

Isotope calibration

In a previous study of Li in kerogen (Teichert *et al.* 2020), NIST SRM 612 was used as a reference material for δ^7Li measurements in coal because there were no known reference materials for Li in a carbonaceous matrix. Therefore, in addition to comparing carbonaceous samples with varying H/C and O/C ratios, another goal of this calibration study was to determine the magnitude of possible matrix

© 2022 The Authors. Geostandards and Geoanalytical Research © 2022 International Association of Geoanalysts

effects on Li isotopes among silicate glass and carbon matrices. The materials listed in Table 1 were implanted with both ^{7}Li and ^{6}Li ions at fluences of 1.0×10^{15} and 1.0×10^{14} atoms cm^{-2}, respectively. The implant energy used was calculated based on the highest density material to be implanted, which was the NIST SRM glass reference material (NIST SRM 612; 2.3 g cm^{-3}; Hervig *et al.* 2006); therefore, a 21 keV implant energy was used for all materials.

SIMS depth profiles of ^{7}Li and ^{6}Li were obtained using the same primary beam types, primary and secondary ion accelerating voltages, raster size and field aperture settings as those described above (*Content calibration*), except that depth profile measurements for the O_2^- primary beam coupled with a 9 kV secondary ion accelerating voltage (Setup 2; Table 3) were not performed. Additionally, no energy filtering was used for isotope ratio measurements, therefore, to avoid oversaturating the electron multiplier detector, entrance and exit slit widths were adjusted to a MRP of ~ 1800 and lower primary beam currents were used (5 nA for Setup 3, 10 nA for Setup 1). Spot measurements were made on an un-implanted NIST SRM 612 reference material using 'standard-sample bracketing' to monitor the IMF during the measurement sessions.

Isotope calibration data reduction: The integrated signals for ^{7}Li and ^{6}Li were used to obtain δ^{7}Li values (in ‰) as follows:

$$\delta^{7}\text{Li} = \left(\frac{R_{\text{Sample}}}{R_{\text{RM}}} - 1\right) \tag{5}$$

where R_{Sample} is the ^{7}Li/^{6}Li signal ratio and R_{RM} is equal to 12.0192 ± 0.0002 (Flesch *et al.* 1973).

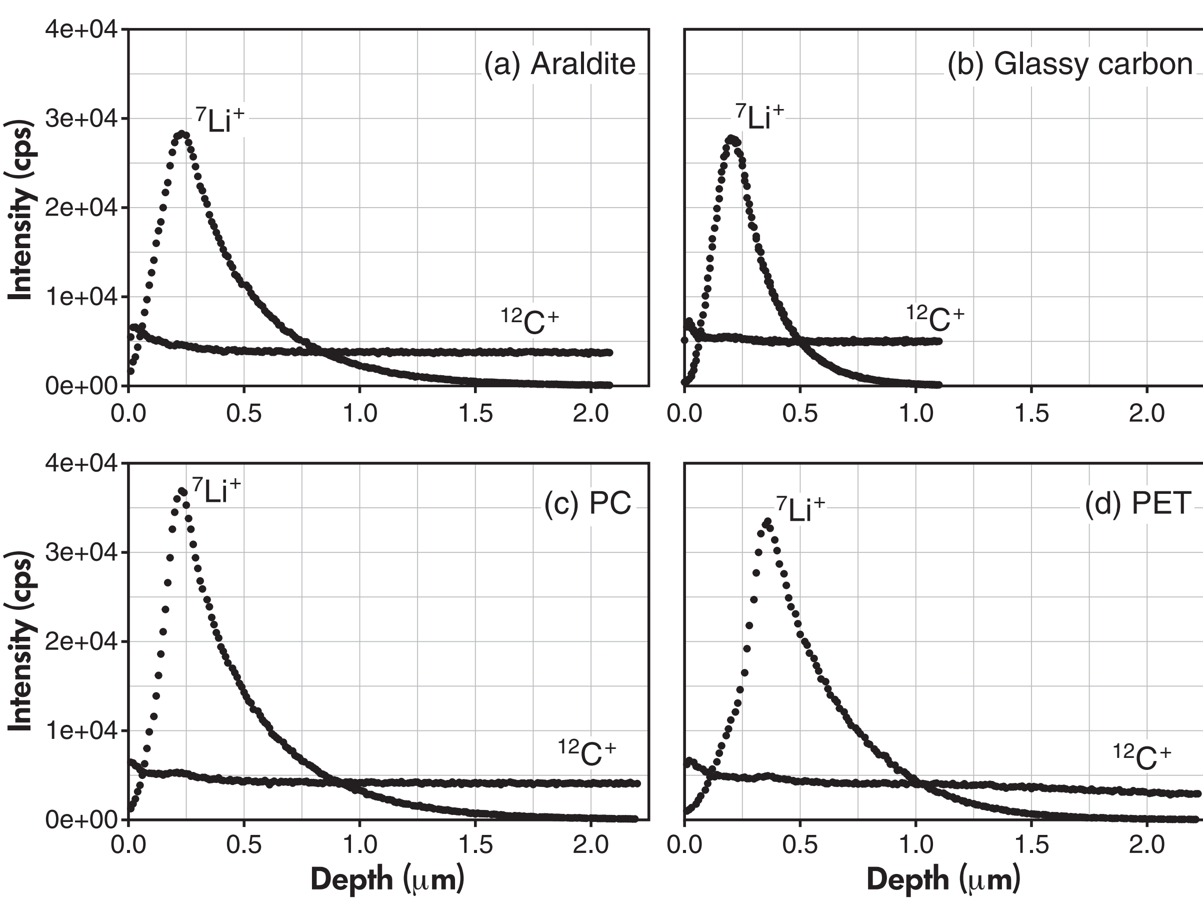

Figure 2. Depth profile measurements into (a) araldite, (b) glassy carbon, (c) PC and (d) PET materials, showing the implant ion (^{7}Li^{+}) and reference ion (^{12}C^{+}) intensities using Setup 2 (O_2^-, 9 kV secondary ion accelerating voltage). Note that ^{12}C^{+} signals were subjected to transient effects near the surface and therefore the first several cycles were not used to determine the mean ^{12}C^{+} count rate. In some materials, ^{12}C^{+} signals would continue to decrease throughout the profile and were the main source of uncertainty in the *K factor calculations. For consistency, the ^{12}C^{+} signal was averaged from where transient effects ended where the ^{7}Li^{+} signal reached 5% of its peak value for all depth profiles.**

 © 2022 The Authors. Geostandards and Geoanalytical Research © 2022 International Association of Geoanalysts

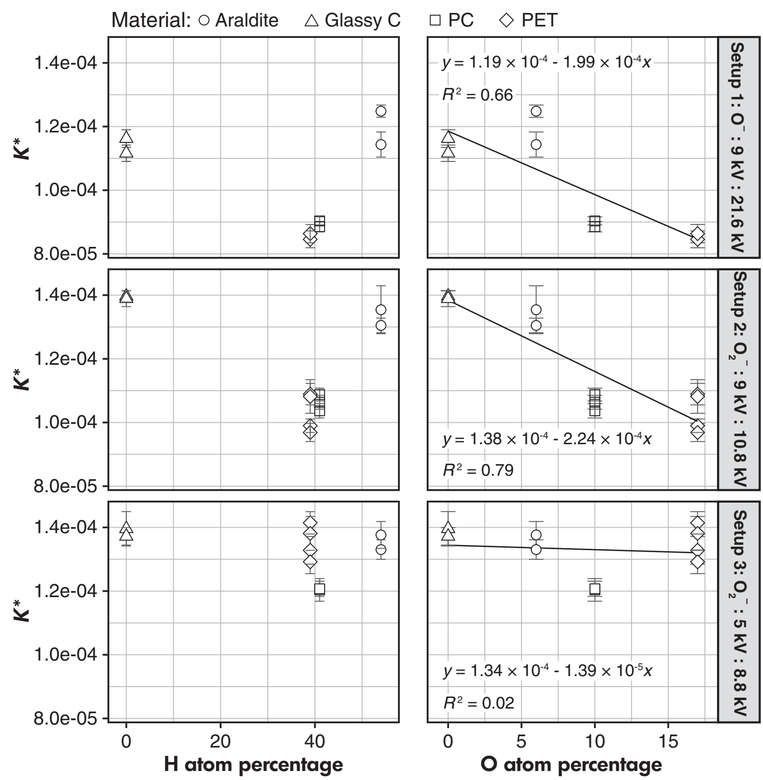

Figure 3. Scatter plots of *K factors are plotted against the atomic abundances of H and O present in polymer and glassy C samples for different instrument setups (primary ion/secondary accelerating voltage/impact energy). See section *Content calibration* for additional setup parameters. $\pm 2s_{\bar{x}}$ of individual analyses is plotted and is the result of uncertainty in the $^{12}C^{+}$ count rate and profilometer depth measurements.**

Table 4.
Mean calculated data and associated uncertainties

	Sputter yield		$^{7}Li^{+}$ useful secondary ion yield	$\pm 2s_{\bar{x}}$	$^{12}C^{+}$ useful secondary ion yield	$\pm 2s_{\bar{x}}$	K^*	$\pm 2s_{\bar{x}}$	*n*
Setup 1									
O^-/9 kV/21.6 kV									
Araldite	3.78	0.28	1.21×10^{-3}	3.6×10^{-5}	1.43×10^{-7}	1.7×10^{-8}	1.20×10^{-4}	1.1×10^{-5}	2
Glassy C	2.03	0.01	1.25×10^{-3}	2.4×10^{-5}	1.40×10^{-7}	8×10^{-9}	1.14×10^{-4}	5×10^{-6}	2
PET	6.61	0.06	1.02×10^{-3}	1.2×10^{-5}	8.6×10^{-8}	2×10^{-9}	8.6×10^{-5}	2×10^{-6}	2
PC	4.66	0.11	1.23×10^{-3}	3.3×10^{-5}	1.08×10^{-7}	7×10^{-10}	9.0×10^{-5}	2×10^{-6}	2
Setup 2									
O_2^-/9 kV/10.8 kV									
Araldite	4.02	0.2	8.8×10^{-4}	3×10^{-6}	1.14×10^{-7}	4×10^{-9}	1.33×10^{-4}	5×10^{-6}	2
Glassy C	2.05	0.01	1.05×10^{-3}	2×10^{-6}	1.44×10^{-7}	1×10^{-9}	1.39×10^{-4}	8×10^{-7}	2
PET	6.64	0.08	8.2×10^{-4}	6.8×10^{-5}	8.3×10^{-8}	2×10^{-9}	1.03×10^{-4}	6×10^{-6}	4
PC	4.95	0.11	9.9×10^{-4}	3.1×10^{-5}	1.03×10^{-7}	8×10^{-10}	1.06×10^{-4}	3×10^{-6}	3
Setup 3									
O_2^-/5 kV/8.8 kV									
Araldite	4.68	0.05	6.0×10^{-4}	3×10^{-6}	7.9×10^{-8}	3×10^{-9}	1.35×10^{-4}	5×10^{-6}	2
Glassy C	2.2	0.05	7.6×10^{-4}	7×10^{-6}	1.03×10^{-7}	3×10^{-9}	1.38×10^{-4}	2×10^{-6}	2
PET	7.06	0.08	5.6×10^{-4}	4.1×10^{-5}	7.4×10^{-8}	4×10^{-9}	1.35×10^{-4}	6×10^{-6}	4
PC	5.37	0.05	7.0×10^{-4}	1×10^{-6}	8.3×10^{-8}	1×10^{-10}	1.21×10^{-4}	4×10^{-7}	2

The mean values of sputter yields, useful secondary ion yields and *K** factors grouped by material and analytical setup.
The uncertainties are $2s_{x}$ determined from the mean values of the number of analyses (*n*).

© 2022 The Authors. Geostandards and Geoanalytical Research © 2022 International Association of Geoanalysts

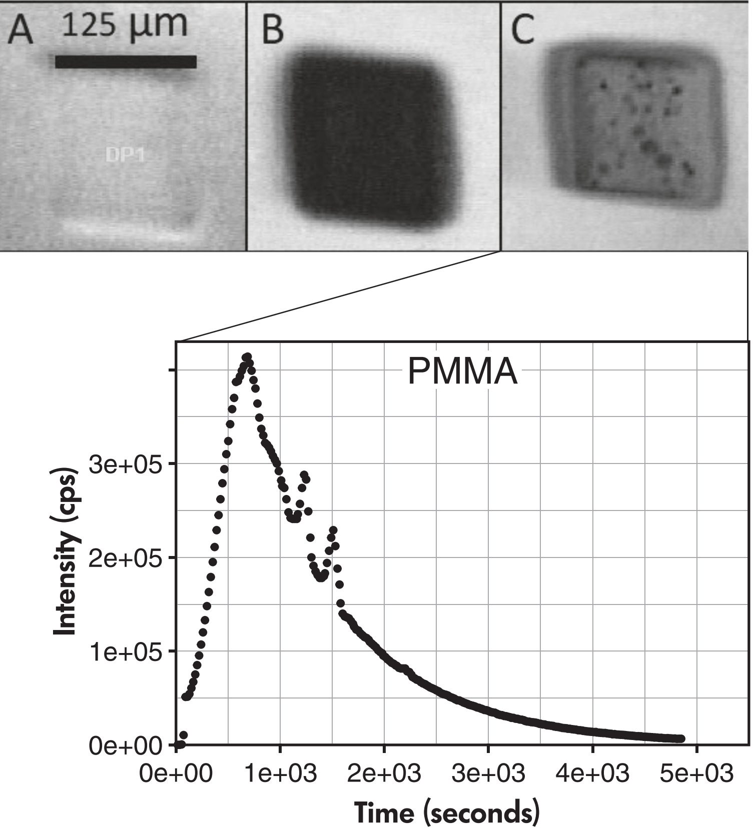

Figure 4. Comparison of analytical craters in different matrices; (a) NIST SRM 612 glass, (b) polycarbonate (PC), (c) polymethacrylate (PMMA). The spots shown in C appear to be bubbles related to melting. The effect of this melting on the $^7Li^+$ implant profile is shown in the PMMA depth profile.

For the NIST SRM 612 glass, the background Li count rate was subtracted from the integrated Li profile. For polymer and glassy carbon samples, there was no significant Li background (< 100 cps). The δ^7Li‰ deviations of each implanted carbonaceous sample from the NIST SRM 612 Li isotope implant reference material (δ^7Li_{612}) were determined with the following expression

$$\delta^7 Li_{612} = \delta^7 Li_{612\ implant\ RM} – \delta^7 Li_{i\ implant\ reference\ material} \quad (6)$$

where $\delta^7Li_{612\ implant\ RM}$ is the δ^7Li value for the NIST SRM 612 implant reference material, and $\delta^7Li_{i\ implant\ RM}$ is δ^7Li for each of the carbonaceous implant reference materials.

A minor correction for differences in backscattering between the NIST SRM 612 glass and the carbonaceous samples was also applied. According to TRIM simulations, during the ion implant process, the NIST SRM 612 glass backscattered approximately 1.4% of the $^7Li^+$ ions and 1.6% of the $^6Li^+$ ions. The carbonaceous materials backscattered less < 0.2% of both Li implant species. Accordingly, we calculated that the implant ratio of the NIST SRM 612 is 1.5‰ larger than for the carbonaceous samples and applied this correction.

Potential problems related to the instantaneous count rate loss when using a secondary ion aperture over a rastered beam (Simons *et al.* 2005) may be approximated by multiplying the mean count rate by the ratio of the rastered area to the apertured area, but this method will overestimate the instantaneous count rate if the beam diameter is larger than the analysed diameter. Another method to calculate the instantaneous count rate loss is to use the dynamic transfer operating system (DTOS) and to calculate the intensity ratio of Li ions at 100% DTOS (where all counts from the raster are focused to a spot) and the 0% DTOS (no electronic gating) as the factor by which to multiply the mean count rate. It is necessary that the diameter of the 100% DTOS beam be roughly equal to the diameter of the primary beam for this correction to be accurate. The second procedure was applied by measuring $^7Li^+$ on the un-implanted NIST SRM 612 RM using both 100% DTOS and 0% DTOS to calculate

© 2022 The Authors. Geostandards and Geoanalytical Research © 2022 International Association of Geoanalysts

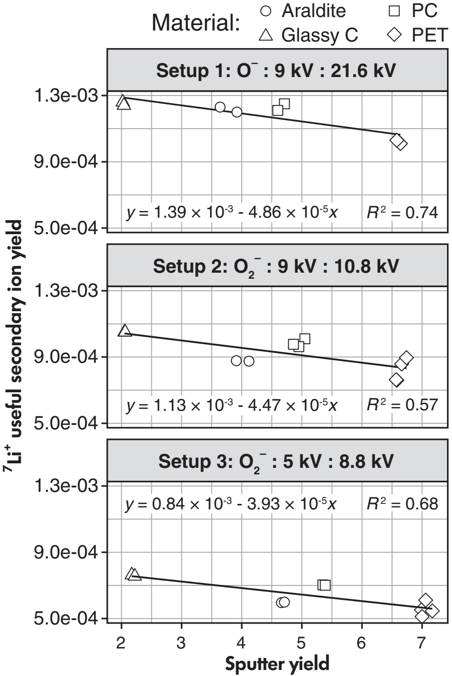

Figure 5. $^7Li^+$ useful secondary ion yields are plotted against the sputter yields for each material and for each analytical setup. See section *Content calibration* for additional setup parameters. Uncertainties ($2s_{\bar{x}}$) for individual useful secondary ion yields are < 5%.

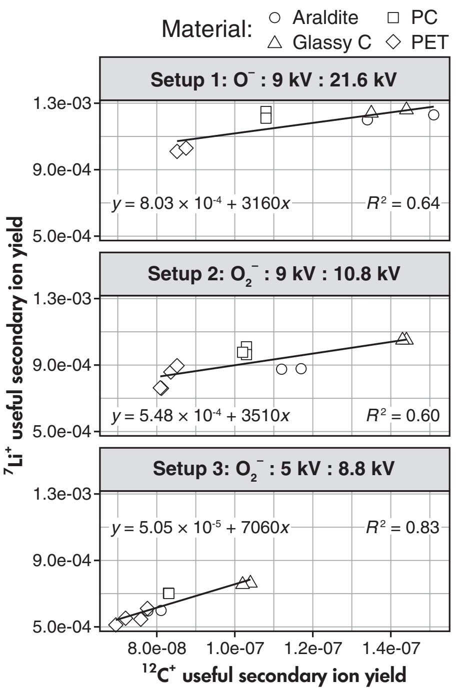

Figure 6. $^7Li^+$ useful secondary ion yields are plotted against the $^{12}C^+$ useful secondary ion yields for each material and analytical setup. See section *Content calibration* for additional setup parameters. Uncertainties ($\pm 2s_{\bar{x}}$) for individual useful secondary ion yields are < 5%.

the factor needed to obtain the instantaneous count rate loss. Once the instantaneous count rate was calculated for each cycle in a given measurement, a correction was made for both Li isotopes by adding count losses to those integrated signals. The count loss correction changed the δ^7Li_{612} by a range of +1 to +18‰ and was applied to all the Li isotope implant reference material measurements but was not necessary for the content calibration because the instantaneous count rate correction was not significant (< 1.5%). Ideally, both isotopes are implanted with the same fluence, so that the instantaneous count losses are the same, and correction is not necessary.

Results and discussion

Lithium content calibration

The secondary ion intensities of $^7Li^+$ and $^{12}C^+$ are plotted against depth in Figure 2 for several depth profile measurements into ion implant reference materials. The *K** calibration factors (Equation 4) for each material are plotted against the atomic abundances of H and O for the different analytical setup conditions (Figure 3). Multiple depth profiles were taken for each material. Table 4 shows the mean *K** factors, sputter yields (atoms sputtered per impinging atom) and $^7Li^+$ and $^{12}C^+$ useful secondary ion yields for each material.

The polymethyl methacrylate (PMMA or Plexiglas), which has the lowest melting point (160 °C) showed evidence of melting (Figure 4) during ion bombardment resulting in unstable secondary ion signals, and therefore, the results from those analyses are not included or discussed further.

For analytical setups 1 and 2, using the 9 kV secondary ion accelerating voltage, the araldite and Glassy C have higher *K** factors than PC and PET resulting in a negative trend between *K** factors and the atomic abundance of O (Figure 3). Despite having a similar trend for the materials, the *K** factors are shifted higher in Setup 2 compared with Setup 1. Even though the same primary and secondary ion accelerating voltages were used in both Setup 1 and 2, the impact energies of the impinging atoms are different because O_2^- ions break into two O atoms when they strike the sample surface, which halves the impact energy of

© 2022 The Authors. Geostandards and Geoanalytical Research © 2022 International Association of Geoanalysts

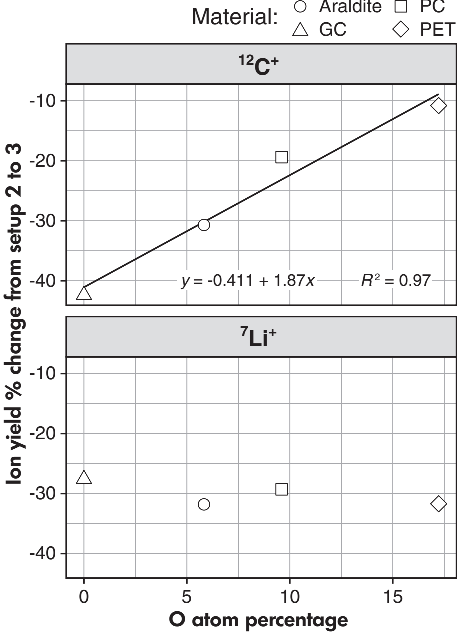

Figure 7. Scatter plots showing the per cent change in the useful secondary ion yields of $^7Li^+$ and $^{12}C^+$ between analysis using a 9 kV (Setup 2) and a 5 kV (Setup 3) secondary ion accelerating voltage. The trend line for $^{12}C^+$ shows how the ^{12}C useful ion yields decreased as a function of sample O content going from setup 2 to setup 3.

each O atom. The lower impact energy of Setup 2 (10.8 keV) compared with Setup 1 (21.6 keV) decreases the depth range of the primary ions and thus sets more surface atoms in motion, resulting in higher sputter yields (Table 4; Figure 5; Sigmund 1969). Conversely, the lower impact energies decrease the surface concentration of the primary ion species (oxygen) implanted into the sample, which is approximately equivalent to the reciprocal of the sputter yield (Liebl 1975, Deline *et al.* 1978b, Williams 1979a). Williams (1979a) found that secondary ion yields are negatively correlated with the sputter yield as demonstrated in this study (Figure 5) because primary oxygen accumulates in the craters, enhancing ionisation due to its high electronegativity.

The *K** calibration factor can also be expressed as the implant ion useful secondary ion yield ($^7Li^+$) relative to the reference ion useful secondary ion yield ($^{12}C^+$) (see section *Content calibration data reduction*):

$$K^* = \left(\frac{\text{Useful } ^{12}\text{C ion yield}}{\text{Useful } ^{7}\text{Li ion yield}}\right) \tag{7}$$

Therefore, increasing the surface concentration of O by primary beam implantation evidently enhances the $^7Li^+$ ion yields by a greater factor than the $^{12}C^+$ ion yields, and this can be seen in Figure 6 and Table 4 by comparing how $^7Li^+$ and $^{12}C^+$ secondary ion useful yields change from Setup 2 to Setup 1 for each material. The trends in Figure 6 suggest that samples with higher O content will have lower *K** factors (i.e., greater sensitivity to $^7Li^+$ relative to $^{12}C^+$) as is observed in Figure 3 for Setups 1 and 2.

Using Setup 3, the mean values for the *K** factors of each material, apart from PC, are within statistical uncertainty. The PC *K** factor is 13% lower than Glassy C with Setup 3, 24% lower with Setup 2 and 21% lower with Setup 1. Therefore, by measuring the carbonaceous samples using a 5 kV

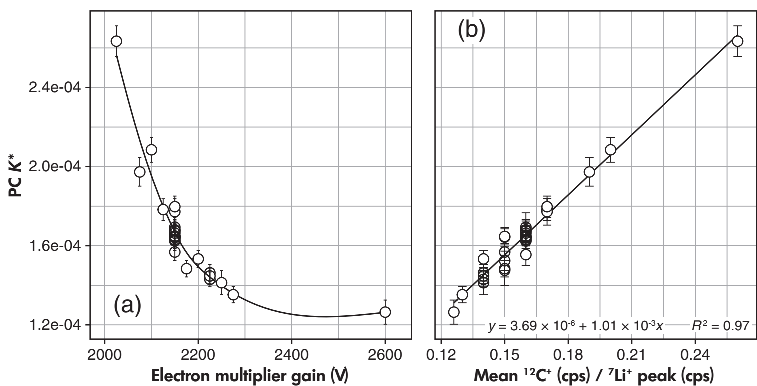

Figure 8. Plot showing the (a) EM gain vs. *K factors on PC and (b) the mean $^{12}C^+/^7Li^+$ peak correlation with *K** factors using Setup 3 (5 kV secondary ion accelerating voltage). Range bars shown are $2s_{\bar{x}}$.**

© 2022 The Authors. Geostandards and Geoanalytical Research © 2022 International Association of Geoanalysts

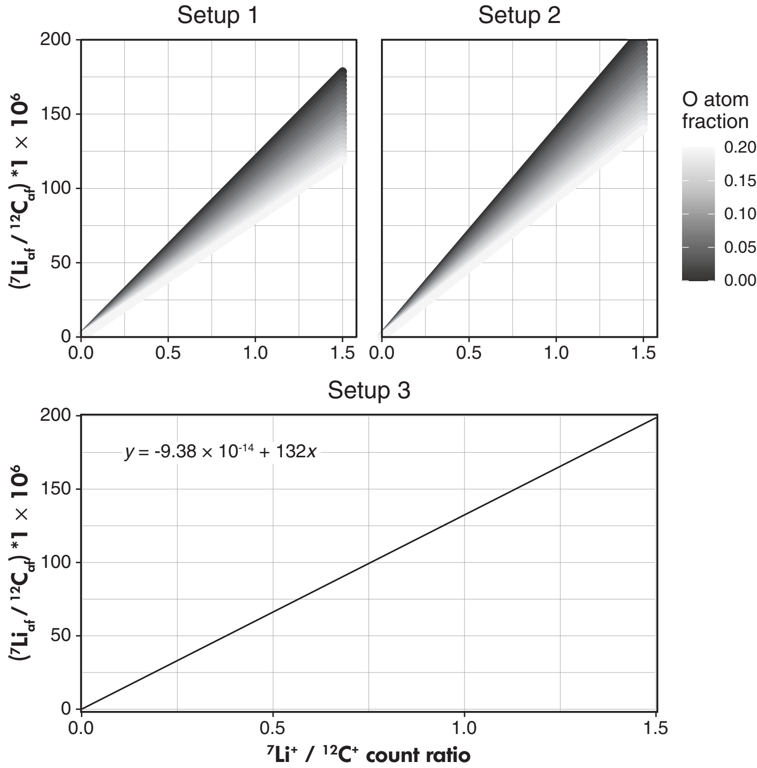

Figure 9. Calibration lines are plotted for each of the three analytical setups used (Table 3). The *x*-axis is the $^{7}Li^{+}/^{12}C^{+}$ count rate on the unknown sample and the *y*-axis is the ^{7}Li atom fraction (af) normalised to the $^{12}C_{af}$ expressed in ppma. For Setups 1 and 2, the calibration is a function of the oxygen atom fraction (O_{af}), calculated from the trend lines shown in Figure 3. The single calibration curve for Setup 3 is derived from the mean of the K^{*} factors for all carbonaceous materials. Multiplication of the *y*-axis value by the $^{12}C_{af}$ of the sample measured gives Li content in ppma.

secondary ion, accelerating voltage one can effectively eliminate matrix effects related to the O contents.

Hervig *et al.* (2006) observed that useful secondary ion yields increased proportionally with secondary ion accelerating voltage in NIST SRM 610 glass. In addition to the lower secondary ion accelerating voltage, Setup 3 also has a lower impact energy (8.8 keV) than the other setups, which also decreases ion yields. Figure 7 shows the per cent change in the useful secondary ion yields as the secondary voltage is increased from 9 to 5 kV secondary ion accelerating voltage. The useful secondary ion yields of $^{7}Li^{+}$ decrease by ~30% for all samples. The $^{12}C^{+}$ useful secondary ion yields, however, decrease as a function of the O content of the sample, with the samples with higher O content having a smaller decrease when changing from Setup 2 to Setup 3. At a 9 kV secondary ion accelerating voltage (Setups 1 and 2), it was observed that the materials with higher O contents had lower K^{*} factors (i.e., Equation 7). That is not observed at a 5 kV secondary ion accelerating voltage (Setup 3), because the useful secondary ion yields of $^{12}C^{+}$ decrease the least in the materials with high O contents (Figure 7); thus, equalising the Useful ^{12}C ion yield/Useful ^{7}Li ion yield ratio (i.e., K^{*} factors) for all materials. It is unclear why the secondary ion accelerating voltage affects the useful ion yields of $^{12}C^{+}$ so significantly, and this question requires further study.

Electron multiplier effects on the Li content calibration factor (K^{*}): Several instrumental parameters including the primary ion current (5–50 nA), sample height (± 15 μm) and immersion lens voltage were tested to determine how each might affect the K^{*} factors, and those parameters were determined to have a negligible effect. The electron multiplier gain has a considerable influence on the K^{*} factors because of the higher detection efficiency of $^{12}C^{+}$ relative to $^{7}Li^{+}$ secondary ions (Zinner *et al.* 1986). It is common for the electron multiplier gain to be adjusted with aging of the detector because the sensitivity of ion conversion to electrons degrades with use (Frank *et al.*

© 2022 The Authors. Geostandards and Geoanalytical Research © 2022 International Association of Geoanalysts

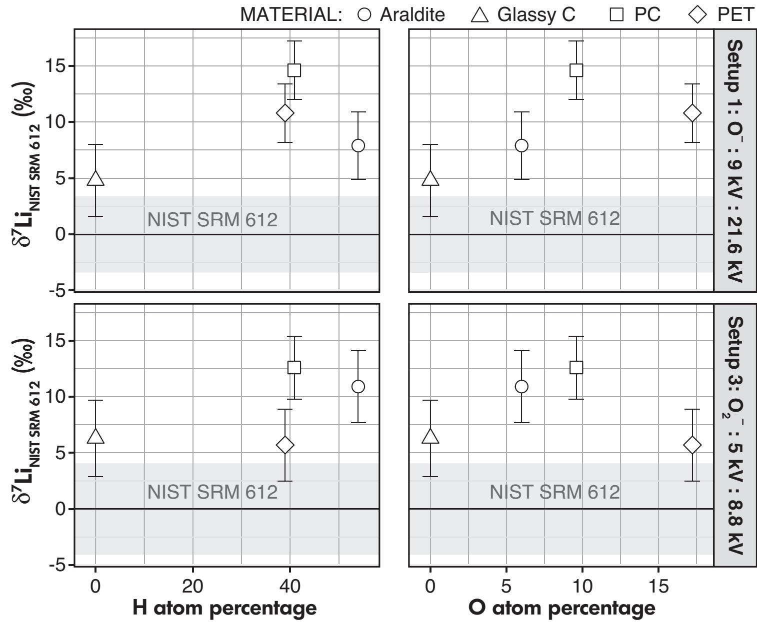

Figure 10. NIST SRM 612 implant reference materials' mean isotope ratio is plotted as the origin of the *y*-axis with the grey region indicating the analytical uncertainty in the measurement. The isotopic deviations from the NIST SRM 612 implant reference materials' isotope ratio (δ^7Li_{612}) are plotted for each sample against H and O atom per cent for instrument Setups 1 and 3. The range bars shown are the sum of $2s_{\bar{x}}$ uncertainty in the IMF and the Poisson Error (P.E.) of the individual analyses of the implant reference materials plotted.

1969); therefore, it is important to maximise the EM response. Figure 8a demonstrates the magnitude of the effect of EM gain on *K** factors, showing a systematic decrease as the EM gain is increased. The *K** factor changes because $^7Li^+$ counts increase relative to $^{12}C^+$ as the detector sensitivity is increased. The *K** factor is linearly correlated with the mean $^{12}C^+/^7Li^+$ peak intensity (Figure 8b); thus, maximising the ratio can be used to set the EM gain.

Application of content calibration: Figure 9 shows calibration curves for the conversion of $^7Li^+/^{12}C^+$ count ratios to the ^7Li atom/^{12}C atom fraction in organic matrices for each of the analytical setups described here. Because Li is typically a trace element in organic materials the atom fraction ratio is multiplied by 1×10^6 to express the ^7Li concentration, in ppm atomic (ppma), in terms of the ^{12}C concentration. Once this value (*y*-axis) is obtained from a given $^7Li^+/^{12}C^+$ count ratio, it can be multiplied by the ^{12}C atom fraction of the unknown to convert to ^7Li ppma for the entire sample, which can then be converted to $\mu g\,g^{-1}$ convenient to geochemical studies.

For Setup 1 and 2, the calibration is a function of sample O content (atom fraction; O_{af}) as well as the $^7Li^+/^{12}C^+$ intensity ratios, whereas the calibration for Setup 3 (using a 5 kV secondary ion accelerating voltage) is a single curve independent of sample O content. It is key to note that these trend lines are accurate only if the electron multiplier detection efficiency is maximised, the MRP is approximately 1000 and ions with 75 ± 20 eV initial kinetic energy are detected. Content calibrations determined here with an IMS-6f may not be directly transferable to different instruments (e.g., NanoSIMS) where secondary ion optics and detection systems differ significantly. Ideally, calibration curves should be determined for different types of SIMS instruments.

Li isotopic calibration

The δ^7Li‰ deviations of each implanted carbonaceous sample from the NIST SRM 612 Li isotope implant reference material (δ^7Li_{612}) are plotted against their atomic abundances of H and O (Figure 10) for analytical setups 1 and 3. Using either analytical setup, the Li isotope calibration in glassy carbon (SPI Glas-22) is within uncertainty of the NIST SRM 612 glass. The carbonaceous matrices are on average +10‰ higher than the NIST SRM 612 silicate glass reference material using both analytical setups. In each case, PC has the largest deviation from the NIST SRM 612 glass reference material. There is no apparent relationship between

 © 2022 The Authors. Geostandards and Geoanalytical Research © 2022 International Association of Geoanalysts

sample H and O contents and the measured Li isotope ratio.

Conclusions

Organic polymer samples were implanted with Li ions to serve as reference materials for SIMS measurements of Li content and isotope ratios in kerogen. SIMS depth profile measurements through Li ion implants were used to calculate a Li content calibration factor (*K**). The results show no matrix effects related to variable H and O contents of the carbonaceous materials using an O_2^- primary ion beam and 5 kV secondary ion accelerating voltage. However, a matrix effect related to sample O content was observed when using an O^- or O_2^- primary beam with a 9 kV secondary ion accelerating voltage. Therefore, at a MRP of ~ 1000, we recommend the use of a 5 kV secondary ion accelerating voltage when measuring Li in organic matrices, to avoid a matrix effect related to sample O content and to improve depth resolution.

For Li isotope calibration reference materials, there is a matrix effect with organic polymer samples having a +10‰ greater δ^7Li‰ than silicate glass (NIST SRM 612) on average; however, glassy C (SPI Glas-22) is within uncertainty of NIST SRM 612 glass. Preparation of implant reference materials as described in this study can provide matrix-matched calibrations for both Li content and Li isotopes in similar organic matrices.

Acknowledgements

We wish to thank the two anonymous reviewers for their thoughtful questions and comments. We thank Leonard Kroko for his valuable advice regarding the feasibility of the various ion implantations and for implanting the materials used in this study. We also thank Intertek Group PLC for performing the CHN analyses of polymer samples for verification of their chemistry.

Funding information

This work was funded by the US National Science Foundation (EAR-1811613) and analytical work was supported by the ASU SIMS Facility funded by (EAR-1819550).

Data availability statement

The data that support the findings of this study are available in Mendeley Data (http://dx.doi.org/10.17632/92tgdmn45y.1) and in the EarthChem data library (https://earthchem.org).

References

Andersen C.A. and Hinthorne J.R. (1972)
Ion microprobe mass analyzer. Science, 175, 853–860.

Befus K.S., Walowski K.J., Hervig R.L. and Cullen J.T. (2020)
Hydrogen isotope composition of a large silicic magma reservoir preserved in quartz-hosted glass inclusions of the Bishop Tuff plinian eruption. Geochemistry Geophysics Geosystems, 21, 22.

Bell D.R., Hervig R.L., Buseck P.R. and Aulbach S. (2009)
Lithium isotope analysis of olivine by SIMS: Calibration of a matrix effect and application to magmatic phenocrysts. Chemical Geology, 258, 5–16.

Burnett D.S., Jurewicz A.J.G., Woolum D.S., Wang J., Paque J.M., Nittler L.R., McKeegan K.D., Humayun M., Hervig R., Heber V.S. and Guan Y. (2015)
Ion implants as matrix-appropriate calibrators for geochemical ion probe analyses. Geostandards and Geoanalytical Research, 39, 265–276.

Deline V.R., Evans C.A. and Williams P. (1978b)
A unified explanation for secondary ion yields. Applied Physics Letters, 33, 578–580.

Deline V.R., Katz W., Evans C.A. and Williams P. (1978a)
Mechanism of the SIMS matrix effect. Applied Physics Letters, 33, 832–835.

Deng R.C. and Williams P. (1989)
Factors affecting precision and accuracy in quantitative analysis by secondary ion mass spectrometry. Analytical Chemistry, 61, 1946–1948.

Farquhar J., Hauri E. and Wang J. (1999)
New insights into carbon fluid chemistry and graphite precipitation: SIMS analysis of granulite facies graphite from Ponmudi, South India. Earth and Planetary Science Letters, 171, 607–621.

Flesch G.D., Anderson A.R. and Svec H.J. (1973)
A secondary isotopic standard for ^{6}Li/^{7}Li determinations. International Journal of Mass Spectrometry, 12, 265–272.

Fletcher I.R., Kilburn M.R. and Rasmussen B. (2008)
NanoSIMS µm-scale *in situ* measurement of ^{13}C/^{12}C in early Precambrian organic matter, with permil precision. International Journal of Mass Spectrometry, 278, 59–68.

Frank L.A., Henderson N.K. and Swisher R.L. (1969)
Degradation of continuous-channel electron multipliers in a laboratory operating environment. Review of Scientific Instruments, 40, 685–689.

Franzreb K., Lörinčík J. and Williams P. (2004)
Quantitative study of oxygen enhancement of sputtered ion yields. I. Argon ion bombardment of a silicon surface with O_2 flood. Surface Science, 573, 291–309.

© 2022 The Authors. Geostandards and Geoanalytical Research © 2022 International Association of Geoanalysts

references

Hauri E.H., Shaw A.M., Wang J., Dixon J.E., King P.L. and Mandeville C. (2006)
Matrix effects in hydrogen isotope analysis of silicate glasses by SIMS. Chemical Geology, 235, 352–365.

Hauri E., Wang J., Dixon J.E., King P.L., Mandeville C. and Newman S. (2002)
SIMS analysis of volatiles in silicate glasses: 1. Calibration, matrix effects and comparisons with FTIR. Chemical Geology, 183, 99–114.

Heber V.S., McKeegan K.D., Burnett D.S., Duprat J., Guan Y., Jurewicz A.J.G., Olinger C.T. and Smith S.P. (2014)
Accurate analysis of shallowly implanted solar wind ions by SIMS backside depth profiling. Chemical Geology, 390, 61–73.

Hervig R.L., Bell D.R., Moore G., Williams L.B., Yamamoto J. and Buseck P.R. (2004)
SIMS analyses for Li isotope ratios: From olivine to clay minerals. In: AGU Fall Meeting Abstracts. American Geophysical Union, Fall Meeting 2004, 51, 593pp.

Hervig R.L., Mazdab F.K., Moore G. and McMillan P.F. (2003)
Analyzing hydrogen (H_2O) in silicate glass by secondary ion mass spectrometry and reflectance Fourier transform infrared spectroscopy. In: De Vivo B. and Bodnar R.J. (eds), Developments in volcanology (Volume 5). Elsevier (Amsterdam, Netherlands), 83–103.

Hervig R.L., Mazdab F.K., Williams P., Guan Y., Huss G.R. and Leshin L.A. (2006)
Useful ion yields for Cameca IMS 3f and 6f SIMS: Limits on quantitative analysis. Chemical Geology, 227, 83–99.

Hofker W.K. (1975)
Implantation of boron in silicon. MSc thesis. Amsterdam University (The Netherlands), 49pp.

Hollocher K. and Ruiz J. (1995)
Major and trace element determinations on NIST glass standard reference materials 611, 612, 614 and 1834 by inductively coupled plasma-mass spectrometry. Geostandards Newsletter, 19, 27–34.

House C.H., Schopf J.W., McKeegan K.D., Coath C.D., Harrison T.M. and Stetter K.O. (2000)
Carbon isotopic composition of individual Precambrian microfossils. Geology, 28, 707–710.

Isa J., Kohl I.E., Liu M.-C., Wasson J.T., Young E.D. and McKeegan K.D. (2017)
Quantification of oxygen isotope SIMS matrix effects in olivine samples: Correlation with sputter rate. Chemical Geology, 458, 14–21.

Jeffcoate A.B., Elliott T., Kasemann S.A., Ionov D., Cooper K. and Brooker R. (2007)
Li isotope fractionation in peridotites and mafic melts. Geochimica et Cosmochimica Acta, 71, 202–218.

Kaminsky F.V., Shilobreeva S.N., Ber B.Y. and Kazantsev DYU (2020)
Quantification of hydrogen in natural diamond by secondary ion mass spectrometry (SIMS). Dokladay Earth Sciences, 494, 699–703.

Kasemann S.A., Jeffcoate A.B. and Elliott T. (2005)
Lithium isotope composition of basalt glass reference material. Analytical Chemistry, 77, 5251–5257.

Kaufman A.J. and Xiao S. (2003)
High CO_2 levels in the Proterozoic atmosphere estimated from analyses of individual microfossils. Nature, 425, 279–282.

Lemarchand E., Chabaux F., Vigier N., Millot R. and Pierret M.-C. (2010)
Lithium isotope systematics in a forested granitic catchment (Strengbach, Vosges Mountains, France). Geochimica et Cosmochimica Acta, 74, 4612–4628.

Leta D.P. and Morrison G.H. (1980)
Ion implantation for *in-situ* quantitative ion microprobe analysis. Analytical Chemistry, 52, 277–280.

Li Y., Wiedenbeck M., Shcheka S. and Keppler H. (2013)
Nitrogen solubility in upper mantle minerals. Earth and Planetary Science Letters, 377–378, 311–323.

Liebl H. (1975)
Secondary-ion mass spectrometry and its use in depth profiling. Journal of Vacuum Science and Technology, 12, 385–391.

McCarthy K., Niemann M., Palmowski D., Peters K. and Stankiewicz A. (2011)
Basic petroleum geochemistry for source rock evaluation. Schlumberger, 23, 32–43.

Mojzsis S.J., Arrhenius G., McKeegan K.D., Harrison T.M., Nutman A.P. and Friend C.R.L. (1996)
Evidence for life on Earth before 3800 million years ago. Nature, 384, 55–59.

Nuñez J., Renslow R., Cliff J.B. and Anderton C.R. (2017)
NanoSIMS for biological applications: Current practices and analyses. Biointerphases, 13, 03B301.

Orphan V.J., House C.H., Hinrichs K.-U., McKeegan K.D. and DeLong E.F. (2001)
Methane-consuming archaea revealed by directly coupled isotopic and phylogenetic analysis. Science, 293, 484–487.

Othmane G., Hull S., Fayek M., Rouxel O., Lahd G.M. and Kyser T.K. (2015)
Hydrogen and copper isotope analysis of turquoise by SIMS: Calibration and matrix effects. Chemical Geology, 395, 41–49.

Regier M.E., Hervig R.L., Myers M.L., Roggensack K. and Wilson C.J.N. (2016)
Analyzing nitrogen in natural and synthetic silicate glasses by secondary ion mass spectrometry. Chemical Geology, 447, 27–39.

© 2022 The Authors. Geostandards and Geoanalytical Research © 2022 International Association of Geoanalysts

references

Sangély L., Chaussidon M., Michels R. and Huault V. (2005)
Microanalysis of carbon isotope composition in organic matter by secondary ion mass spectrometry. Chemical Geology, 223, 179–195.

Shimizu N. (1979)
Energy filtering and quantitative SIMS analysis of silicates for major and trace elements. In: Benninghoven A., Evans C.A., Powell R.A., Shimizu R. and Storms H.A. (eds), Secondary ion mass spectrometry SIMS II. Springer (Berlin, Heidelberg), 62–63.

Sigmund P. (1969)
Theory of sputtering. I. Sputtering yield of amorphous and polycrystalline targets. Physics Review, 187, 768.

Simons D.S., Chi P.H. and Kim K.J. (2005)
Quantitative measurement of arsenic implant dose by SIMS. Journal of Surface Analysis, 12, 157–160.

Steele R.C.J., Heber V.S. and McKeegan K.D. (2017)
Matrix effects on the relative sensitivity factors for manganese and chromium during ion microprobe analysis of carbonate: Implications for early Solar System chronology. Geochimica et Cosmochimica Acta, 201, 245–259.

Teichert Z., Bose M. and Williams L.B. (2020)
Lithium isotope compositions of U.S. coals and source rocks: Potential tracer of hydrocarbons. Chemical Geology, 549, 119694.

Tonarini S., Pennisi M. and Leeman W.P. (1997)
Precise boron isotopic analysis of complex silicate (rock) samples using alkali carbonate fusion and ion-exchange separation. Chemical Geology, 142, 129–137.

Van Krevelen D.W. (1950)
Graphical-statistical method for the study of structure and reaction processes of coal. Fuel, 29, 269–284.

Van Krevelen D.W. (1961)
Coal (1st edition). Elsevier (Amsterdam), 514pp.

Van Krevelen D.W. and Schuyer J. (1957)
Coal science. Elsevier (Amsterdam), 352pp.

Williams L.B. and Bose M. (2018)
Measurements of the lithium isotope heterogeneity in coals and kerogen indicate an unrecognized lithium contribution to the global geochemical cycles. Clay Minerals Society 55th Annual Conference, Urbana (IL), June 2018.

Williams L.B., Clauer N.C. and Hervig R.L. (2012)
Light stable isotope microanalysis of clays in sedimentary rocks. In: Sylvester P. (ed.), Quantitative mineralogy and microanalysis of sediments and sedimentary rocks. Mineralogical Association of Canada Short Course, 42, 55–73.

Williams L.B., Crawford E.W. and Hervig R.L. (2015)
Tracing hydrocarbons in gas shale using lithium and boron isotopes: Denver Basin USA, Wattenberg gas field. Chemical Geology, 417, 404–413.

Williams L.B., Środoń J., Huff W.D., Clauer N. and Hervig R.L. (2013)
Light element distributions (N, B, Li) in Baltic Basin bentonites record organic sources. Geochimica et Cosmochimica Acta, 120, 582–599.

Williams P. (1979a)
Current problems in low energy ion beam materials analysis with SIMS. IEEE Transactions on Nuclear Science, 26, 1807–1811.

Williams P. (1979b)
The sputtering process and sputtered ion emission. Surface Science, 90, 588–634.

Williams P., Stika K.M., Davies J.A. and Jackman T.E. (1983)
Quantitative SIMS analysis of hydrogenated amorphous silicon using superimposed deuterium implant standards. Nuclear Instruments and Methods in Physics Research, 218, 299–302.

Wilson G.C. and Long J.V.P. (1982)
SIMS analysis of lithium: Ion implantation and matrix effects. International Journal of Mass Spectrometry and Ion Physics, 42, 63–75.

Wilson R.G., Stevie F.A. and Magee C.W. (1989)
Secondary ion mass spectrometry: A practical handbook for depth profiling and bulk impurity analysis. Wiley (New York), 1–384.

Ziegler J.F., Ziegler M.D. and Biersack J.P. (2010)
SRIM – The stopping and range of ions in matter (2010). Nuclear Instruments and Methods in Physics Research Section B, 268, 1818–1823.

Zinner E., Fahey A.J. and McKeegan K.D. (1986)
Characterization of electron multipliers by charge distributions. In: Benninghoven A., Colton R.J., Simons D.S. and Werner H.W. (eds), Secondary ion mass spectrometry SIMS V. Springer Series in Chemical Physics. Springer (Berlin, Heidelberg), 170–172.

Zinner E. and Walker R.M. (1975)
Ion-probe studies of artificially implanted ions in lunar samples. In: Proceedings of the sixth Lunar Science Conference (Houston, Texas), 17pp.

Zinner E., Walker R.M., Chaumont J. and Dran J.C. (1976)
Ion probe analysis of artificially implanted ions in terrestrial samples and surface enhanced ions in lunar sample 76215,77. In: Merrill R.B. (ed.), Proceedings of the seventh Lunar Science Conference (Houston, Texas), 32pp.

Supporting information

The following supporting information may be found in the online version of this article:

Appendix S1. Absolute calibrations of implant fluences.

Appendix S2. Calculation of sputter yield and useful secondary ion yield.

This material is available in http://onlinelibrary.wiley.com/doi/10.1111/ggr.12415/abstract (This link will take you to the article abstract).

© 2022 The Authors. Geostandards and Geoanalytical Research © 2022 International Association of Geoanalysts